In vitro living system for streaming flow rectification

Zhi Dou [1,*] Liu Hong [1,*] Songyuan Cui [1,*] Zhengwei Li,[2,3,*] Fan Kiat Chan [1] Yashraj Bhosale,[1] Onur Aydin,[1] Kai-yu Huang [4] Hyunjoon Kong,[4,5,6] Gabriel Juarez [1] M. Taher A. Saif,[1,6] Leonardo P. Chamorro [1,7,8,9] and Mattia Gazzola [1,6,10,†]

[1]*Department of Mechanical Science and Engineering, University of Illinois at Urbana-Champaign, Urbana, Illinois 61801, USA*
[2]*Department of Biomedical Engineering, University of Houston, Texas 77204, USA*
[3]*Department of Biomedical Science, University of Houston, Texas 77204, USA*
[4]*Department of Chemical and Biomolecular Engineering, University of Illinois at Urbana-Champaign, Urbana, Illinois 61801, USA*
[5]*KU-KIST Graduate School of Converging Science and Technology, Korea University, Seoul 02841, South Korea*
[6]*Carl R. Woese Institute for Genomic Biology, University of Illinois at Urbana-Champaign, Urbana, Illinois 61801, USA*
[7]*Department of Aerospace Engineering, University of Illinois at Urbana-Champaign, Urbana, Illinois 61801, USA*
[8]*Department of Civil and Environmental Engineering, University of Illinois at Urbana-Champaign, Urbana, Illinois 61801, USA*
[9]*Department of Earth Science and Environmental Change, University of Illinois at Urbana-Champaign, Urbana, Illinois 61801, USA*
[10]*National Center for Supercomputing Applications, University of Illinois at Urbana-Champaign, Urbana, Illinois 61801, USA*

(Received 30 November 2023; accepted 11 June 2025; published 8 July 2025)

Small—but finite—fluid inertia can be leveraged to generate steady flows out of liquid vibrations around an immersed interface. In engineering, external high-frequency drivers (10^2–10^5 Hz) allow this inertial rectification phenomenon, known as viscous streaming, to be employed in micron-scale devices for precise flow control, particle manipulation, and spatially controlled chemistry. However, beyond artificial settings, streaming has been hypothesized to be accessible by larger-scale biological systems pertaining to lower frequencies. Then millimeter-size organisms that oscillate or pulsate cilia and appendages in the 1 to 10 Hz range may be able to *endogenously* rectify surrounding flows, for feeding or locomotion, removing the need for external actuators, tethers, or tubing. Motivated by this potential for bio-hybrid robotic applications and biophysical exploration, here we demonstrate an *in vitro* living system able to produce streaming flows endogenously, autonomously, and unassisted. Computationally informed, our biological device generates oscillatory flows through the cyclic contractions of an engineered muscle tissue, shaped in the form of a torus and suspended in fluid within a microparticle image velocimetry setup. Flow patterns consistent with streaming simulations are observed for low-frequency muscle contractions (2–4 Hz), either spontaneous or light-induced, illustrating system autonomy and controllability, respectively. Thus, by connecting tissue engineering with hydrodynamics, this work provides experimental evidence of biologically powered streaming in untethered, millimeter-scale living systems, endowing bio-hybrid technology with inertial microfluidic capabilities. It also illustrates the potential of combining bio-hybrid platforms and simulations to advance both biophysical understanding and fluid mechanics.

DOI: 10.1103/4fzg-vn1v

I. INTRODUCTION

When a liquid vibrates around an immersed small feature, a solid inclusion, or a bubble, fluid inertia and local concentration of stresses conspire to produce a steady flow out of the underlying unsteady field. This inertial rectification phenomenon, known as viscous streaming [1–3], represents an efficient and robust flow machinery to manipulate fluid, suspended particles, and chemicals [4–7]. Depending on oscillation frequency, kinematic viscosity, body size, and shape, a variety of streaming flow topologies can be generated [8–11], conveniently partitioning the fluid domain into neatly separated recirculating regions.

Microfluidics has most prominently capitalized on viscous streaming for particle [11–13] and cell transport [14], sorting [15], separation [16], or concentration [17], as well as for chemical mixing [4]. Due to the miniaturization focus and use of micron-scale features [15,18], these devices must employ high-flow oscillation frequencies (10^2–10^5 Hz) typically realized through an external driver, for example, a loudspeaker or a piezo stack [19,20]. Microscale artificial settings and high-frequency actuation have thus come to define viscous streaming.

However, viscous streaming has also been hypothesized to be accessible by biological systems of larger scale, operating at lower frequencies. Then, a multitude of millimeter-scale aquatic creatures that oscillate or pulsate cilia and appendages in the ∼1–10 Hz range may be able to autonomously rectify surrounding flows, for feeding or locomotion. Large bacteria

*These authors contributed equally to this work.
†Contact author: mgazzola@illinois.edu

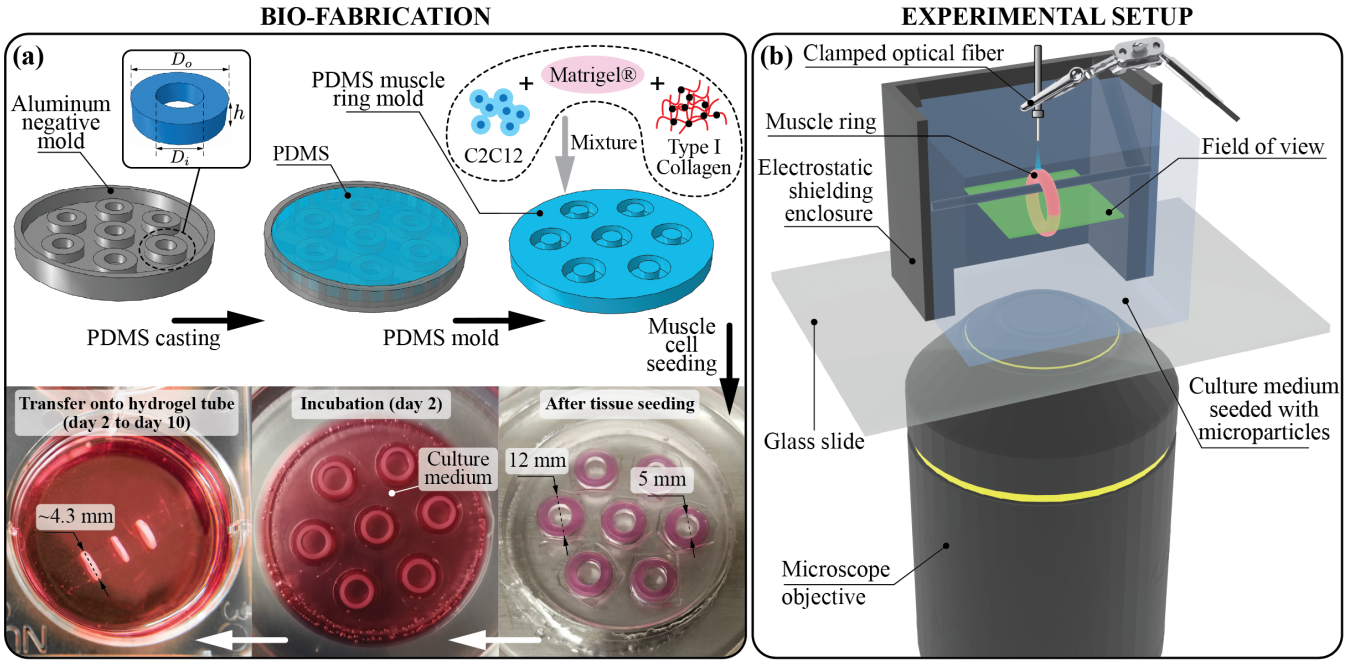

FIG. 1. Bio-fabrication of muscle rings and streaming experimental setup. (a) An aluminum negative mold with torus extrusions of inner diameter $D_i = 5\,\text{mm}$, outer diameter $D_o = 12\,\text{mm}$, and depth $h = 3\,\text{mm}$ is machined. These extrusions define the dimensions of the wells in the PDMS mold. PDMS precursor is poured into the mold and allowed to polymerize at 60 °C. After sterilizing and functionalizing the surface of the detached PDMS mold [42], a mixture containing muscle cells, Matrigel ECM, and type I collagen is injected into the mold, and culture media is added after the cell-gel mixture has polymerized at 37 °C. When the rings have compacted for 2 days, they are transferred onto hydrogel tubes for differentiation until experiment. (b) A machined aluminum enclosure that is open on both top and bottom is glued onto a microscope glass slide and filled with cell culture media mixed with polystyrene tracer particles of diameter 6–8 μm and specific gravity of 1.05. The inner dimension of the enclosure is 1 cm × 1 cm, and two of its opposing walls present cutouts at their centers, to hold a thin aluminum rod (1 mm diameter). For experiments, a muscle ring is transferred from the hydrogel tube onto the rod and suspended in the middle of the box. The entire apparatus is secured on the stage of a microscope, integrated with a cell culture incubator with dark, opaque panels and a high-speed camera focused on the midplane of the ring for recording. For optical stimulation, the tip of an optical fiber connected to a laser diode is placed above the enclosure to produce light pulses.

[21] and larvae [22] have been indeed linked to flow patterns and velocities ($\sim 10^1$–10^2 μm/s) consistent with streaming.

Here, with an eye to micro/bio-robotic applications [23–34] where rectification may be leveraged for local flow manipulation, we investigate the possibility of generating streaming via a living biomimicry, engineered *in vitro* out of muscle cells [Fig. 1(a)] and integrated within a microparticle image velocimetry (μPIV) system [Fig. 1(b)].

The resulting bio-hybrid platform proves to be convenient for our inquiry. Indeed, using wild-type C2C12 skeletal muscle cells, engineered muscle tissues contract spontaneously at a natural frequency [33–38], leading to a simple design where oscillations are self-powered and thus removing the need for external drivers, wires, or tubings. The possibility of rendering muscle cells light-sensitive [39] further provides the option of noninvasively controlling actuation frequency via optical inputs [26,40], ridding the flow field of disturbances caused by otherwise electric stimulation. Additionally, by pouring cells and extracellular matrix (ECM) in a mold [Fig. 1(a)], engineered muscles of different geometry/topology can be formed [41], allowing significant design freedom.

We then realize our freely contracting device in toroidal shape and suspend it in bulk liquid by simply hanging it to a thin submerged horizontal rod [Fig. 1(b)], thus preserving flow three-dimensionality. Computationally informed, this ring-shaped streamer made of skeletal muscle cells is shown to generate streaming flows. The streamer works autonomously through its spontaneous contraction or in a remotely controlled fashion via optical stimulation, demonstrating untethered, biological, millimeter-scale flow rectification. This device is shown to achieve streaming velocities on the scale of ∼10 μm/s, consistent with theoretically and computationally predicted flow strengths, but nonetheless weak compared with microfluidic devices that use externally induced high-frequency vibrations [14,15]. Despite this limitation, our work demonstrates the design, implementation, and control of streaming rectification in a bio-hybrid context. It thus paves the way to outfitting bio-hybrid robots, whose actuation capabilities are continually being improved, with flow streaming capabilities for particles, cells, and nutrients sorting [7,15], mixing [4], or transport [14], adding new complementary functionalities to walking [24–27], swimming [23,28–30], gripping [31,32], or pumping [33,34] abilities. Further, this study underscores the potential utility of bio-hybrid platforms for biophysical and fluid mechanic insight.

II. SETUP

Fundamentals of viscous streaming. Viscous streaming [1,3], an inertial phenomenon, arises when a small feature

(typically a solid inclusion or a microbubble) of characteristic length a, is immersed in a liquid of kinematic viscosity ν, that oscillates with angular frequency ω and amplitude A, subject to the constraint $\epsilon := A/a \ll 1$. In the present context, a is defined as the length of the semimajor axis of the muscle toroidal cross section. The amplitude A is instead defined as half of the average peak-to-peak displacement exhibited by the outer radius of the oscillating torus. We note that we consider the average because in experiments the bio-hybrid streamer will not present perfectly uniform deformations [see Fig. 2(k)]. Inertial rectification, facilitated by stress concentration at the boundaries of the immersed body, results in steady flows that can be effectively leveraged to manipulate fluid, suspended particles, and chemicals [4–7,11]. For simple geometries of uniform curvature (cylinders, spheres), viscous streaming flows have been theoretically, computationally, and experimentally well characterized as a function of the Stokes layer thickness $\delta_{\mathrm{AC}} = O(\sqrt{\nu/\omega})$ and length scale a [1,2,6,10,43]. More recently, the use of multicurvature streaming bodies has revealed rich flow repertoires, furthering opportunities in transport, separation, and assembly [7,9–11,44].

Biostreamer fabrication and flow imaging integration. We aim to build a millimeter-scale, 3D muscle tissue to harvest contractile motions for the generation of oscillatory flows. All the while, the geometry of the tissue itself is selected and leveraged to modulate identifiable streaming fields and facilitate biofabrication, μPIV imaging, and flow analysis.

Here skeletal muscle myoblasts are chosen for their ability to form 3D tissue and fuse into muscle fibers (myotubes) that align spontaneously along stress fields, thus providing directed contractions [45]. This can be achieved by allowing the tissue to anchor on a pair of posts [23,46], providing axial tension thus longitudinal alignment and contraction, or by letting the tissue wrap around a cylindrical core [47], generating tangential stresses and thus tangentially aligned fibers. These, upon contraction, cause the circumference of the tissue to shorten, resulting overall in radial actuation [33,34].

The latter approach is particularly suited to our investigation [Fig. 1(a)]. Indeed, the cylindrical inner core minimizes uneven stress distributions, favoring regular fiber organization, tissue shape, and uniform radial contractions. This, in turn, is conducive of reproducible flow responses. Further, geometric axisymmetry implies the existence of a midplane where the flow becomes 2D, simplifying flow imaging and analysis. Finally, a ring shape can be conveniently suspended in bulk liquid by simply sliding it onto a thin submerged rod [Fig. 1(b)].

To fabricate our muscle ring [Fig. 1(a)], a polydimethylsiloxane (PDMS) mold is first created by pouring liquid precursor into a machined negative mold and allowing it to polymerize. A mixture of C2C12 mouse skeletal muscle myoblasts, ECM, and type I collagen is then cast into the PDMS mold, where the myoblast-laden gel compacts into rings [48]. This composition has been previously shown to lead to robust muscle tissues for application in robotic swimmers[23], valveless pumps [33,34], and neuromuscular actuators [46]. The rings thus created are subsequently transferred onto a hydrogel tube submerged in culture medium, to induce differentiation during which contractile myotubes form and align. Because of hydrogel tube compliance and the muscle internal tension, the diameter of the toroidal muscle tissue typically shrinks by ∼1–2 mm, before stabilizing [33,34].

For flow measurement and analysis, a tailored μPIV system is realized [Fig. 1(b)]. A rectangular aluminum enclosure is machine fabricated and bonded on a glass slide to hold culture medium laden with tracer particles of diameter 6–8 μm. Besides serving as a container, the aluminum box also shields the tracers from external electric fields, minimizing drift caused by their slight negative charge. Two of the box opposing walls present cutouts at their centers to hold a thin aluminum rod onto which the muscle ring is slid. The box has inner dimensions of 1 cm × 1 cm. This choice is dictated by the need to minimize convection, which is observed to be significant (compared to expected streaming velocities) for larger volumes. A direct consequence of using a relatively small box is that flow boundary effects come into play. Nonetheless, we note that streaming is robust to moderate confinement, as demonstrated in periodic lattices [7] both experimentally and numerically. We thus expect that an eventual streaming field generated by a (sufficiently small) muscle ring will be topologically unaffected by the presence of the walls, although we do anticipate a geometric compression of the main flow structures towards the center of the enclosure. This, in turn, may facilitate flow visualization. Indeed, by bringing characteristic flow features closer together, the area to be imaged is reduced, allowing improved resolution and μPIV reconstruction accuracy.

The box and glass slide are mounted on the x-y translation stage of an Olympus IX81 inverted microscope equipped with a 2× objective. The differentiated biostreamer is then transferred into the μPIV system, and we adjust the stage such that the muscle ring is at the center of the field of view. We focus the microscope to the midplane of the toroidal tissue. A Hamamatsu digital camera connected to the microscope is utilized to capture images at 50 Hz, which are paired with a five-frame step size and integrated with spatial cross-correlation to produce velocity field data [49,50]. The biostreamer is thus allowed to contract spontaneously, or upon stimulation by an external optical fiber setup, generating an oscillatory flow in its surrounding. In the case of optical stimulation, tissue biofabrication entails the use of C2C12 cells with a mutated variant of the blue light-sensitive ion channel, channelrhodopsin-2 (ChR2). Myotubes differentiated from these myoblasts selectively respond to precise light wavelengths, in our case 470 nm [26]. To reach the illumination intensity required for muscle contraction [51–53], we connect the fiber to a laser diode source producing light pulses of intensity 1.6 $\mathrm{mW/mm^2}$. The specific combination of light wavelength and intensity prevents the μPIV illumination system from interfering with the biostreamer activity (see the Supplemental Material [42]).

III. RESULTS

Computational design of the biostreamer. Streaming literature has almost exclusively examined the use of genus-0 bodies (i.e., without holes), unlike our muscle ring (genus-1). While in a recent instance [8,9] streaming by a torus was computationally investigated for externally driven flow

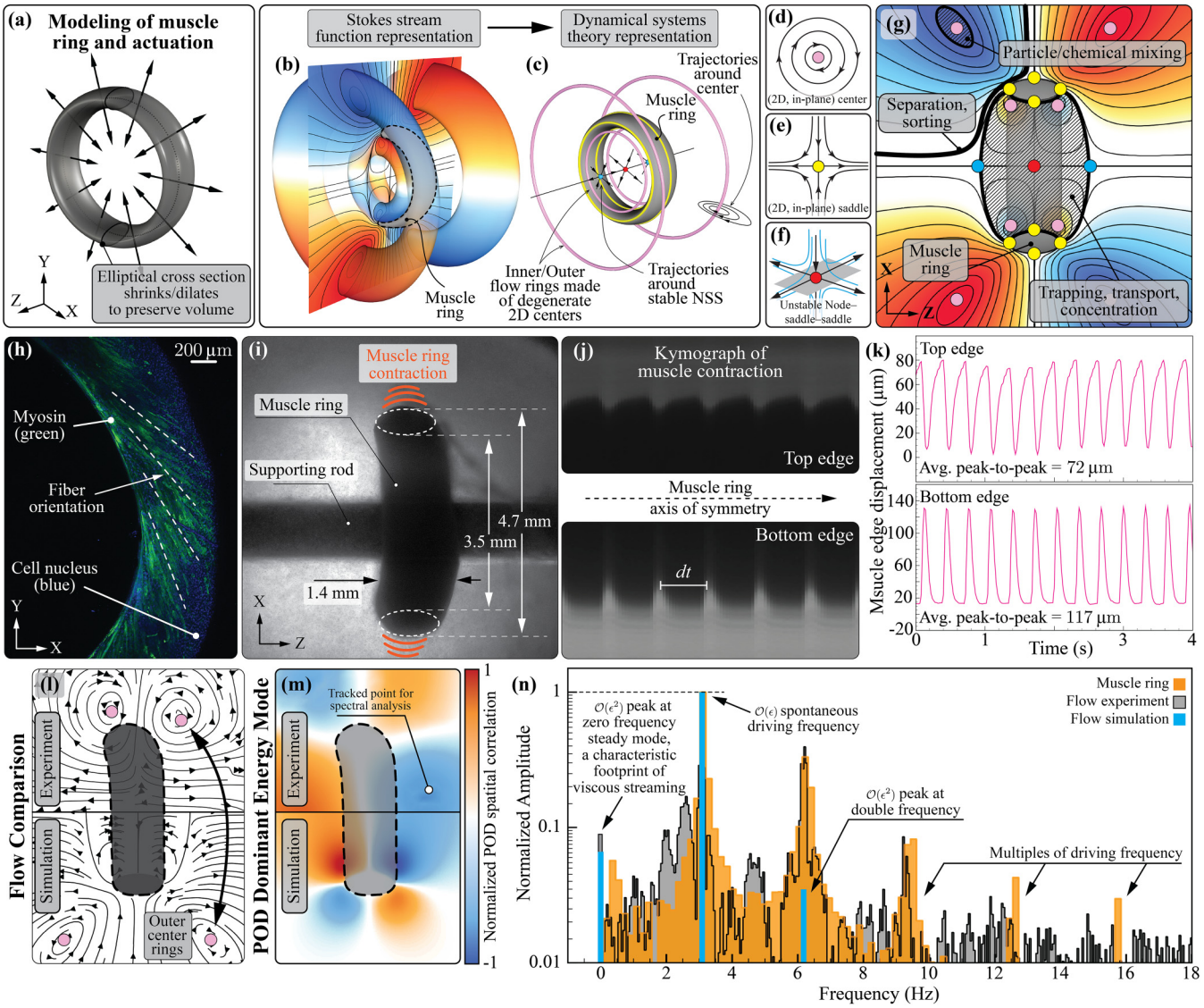

FIG. 2. Computational design of the biostreamer and autonomous streaming. (a) Modeling of the muscle ring and its radial contractions. The computational muscle ring and surrounding liquid environment are characterized, consistent with experiments, by the nondimensional Stokes layer thickness $\delta_{AC}/a = 0.11$, where the length scale a is the depth of the muscle ring. (b), (c) Numerical simulation of the streaming flow around the muscle ring. The visualization of the flow field is presented using two different methods: (b) Stokes stream function and (c) dynamical system representation. (d)–(f) Observed critical points from simulation and illustrations of their corresponding local flow patterns. (g) Expected flow structure at the midplane of the muscle ring from simulation. Critical points are marked by circles with colors corresponding to (d)–(f). Color contours on the presented plane indicate regions of clockwise (blue) and counterclockwise (orange) recirculating fluid. Regions near the critical points where potential particle manipulations can be achieved are encircled in bold lines. (h) Confocal fluorescent z-stack image of a section of a muscle ring showing the circumferentially aligned myotubes (green) and cell nuclei (blue). (i) Bright-field image showing the muscle ring hanging on the thin rod. The ring has measured inner diameter of 3.5 mm, outer diameter 4.7 mm, and depth 1.4 mm. Orange curves illustrate the radial muscle contractions. (j) Kymograph of the top and bottom edge of the muscle ring showing its periodic contractions over 2 seconds. (k) Plots of the top and bottom edge displacement due to muscle actuation over 4 s; valleys in the top plot and peaks in the bottom plot correspond to the fully contracted configuration of the toroidal muscle. We also note that the nondimensional oscillation amplitude input in simulations is set to match the experimentally determined parameter $\epsilon = 0.0675$. This parameter is computed by averaging the top and bottom amplitudes, which in turn are defined as half of the peak-to-peak displacements. (l) Time-averaged streamlines of the upper half of the muscle ring from experiment juxtaposed with streamlines of the lower half of the muscle ring from numerical simulation, showing the matching centers and recirculating regions. (m) Dominant first POD mode extracted using x velocity components (u) from experiments (upper half) juxtaposed with those from simulations (lower half), demonstrating coherent regions from comparatively high correlation zones (flow locations of the same color indicate that local fluid particles move coherently in a correlated fashion; orange/blue colors indicate positive and negative values; the change in sign indicates an opposite sense of motion). The location used for obtaining the experimental flow spectrum is marked. Similar results are observed when analyzing at other flow locations [Supplemental Fig. 3(b) [42]] and when considering the y velocity component v (Supplemental Fig. 3(d) [42]]. (n) Frequency spectrum of the experimental flow (u), simulated flow, and muscle actuation. The normalized amplitude is presented on a logarithmic scale.

oscillations (perpendicular to the body axis of symmetry), no experimental validations have been presented to date and no radial self-contractions have been considered so far. Such limited guidance from literature complicates determining the design of our system, where 3D skeletal muscle constructs can be realized in a range of sizes and operated in a variety of conditions. Viable muscle rings have been indeed reported with (inner) diameters ranging from 0.5 mm to 14 mm [25,33,34,54,55], and wall thicknesses between 0.5 mm and 4 mm [25,55]. Spontaneous contractions have been found to occur within 1 Hz to 10 Hz, and oscillation amplitudes have been observed to vary between 20 μm and 500 μm. [25,33,34]. Additionally, optogenetic C2C12 muscle tissues have been shown to produce consistent force responses to optical control up to ∼5 Hz light stimulation [26].

Thus, to provide insight into the behavior of our coupled flow-muscle system, and in search of design solutions able to robustly generate streaming, we resort to numerical simulation, considering biostreamers within the above outlined, realizable parameters and within the constraints of our μPIV apparatus. We model the muscle ring as a solid undergoing prescribed radial oscillations [while conserving volume, Fig. 2(a)], immersed in an incompressible viscous fluid of unbounded domain. The coupled system is numerically discretized and simulated using a vortex method coupled with Brinkmann penalization [42], an approach [56] demonstrated in a variety of settings [56–61], including streaming [9–11].

Simulations revealed that ring-shaped, radially contracting biostreamers can indeed produce inertial rectification, giving rise to a steady flow of complex topology whose quantitative details vary depending on muscle geometry and actuation properties. A representative instance is reported in Figs. 2(b)–2(g). On the left [Fig. 2(b)], isosurfaces of the time-averaged Stokes stream function (blue and orange representing clockwise and counterclockwise flow rotations) highlight the presence of four recirculating annular regions (two on each side of the muscle ring). Two large regions are found to envelop the biostreamer, while a pair of smaller, nested ones approximately lie within the muscle itself. On the right [Fig. 2(c)] is the corresponding dynamical representation, whereby critical points (characterized by zero velocity) are extracted from the flow and classified based on their stability properties (through the Jacobian of the local velocity field).

The flow is found to be organized around four types of critical points: centers [pink, Fig. 2(d)], saddles (yellow, Fig. 2(e)], and attractive (blue)/repulsive (red) node-saddle-saddle [NSS, Fig. 2(f)]. In our axisymmetric case, both centers and saddles are 2D degenerate [62], since the surrounding local flow has no out-of-plane (i.e., azimuthal) component. These degenerate points, when mapped to 3D space, form four continuous center-rings (pink) and four continuous saddle-rings (yellow), as illustrated in Fig. 2(c). They collectively define the four annular recirculating regions described above.

The computationally extracted flow skeleton underscores the structures that are most likely to be captured experimentally. A streamfunction slice through the midplane [Fig. 2(g)] idealizes experimental visualization conditions and provides intuition. The locations at which the rings cross the midplane are identified by dots of corresponding colors, elucidating the role of centers and saddles in shaping the flow while highlighting their practical utility. Specifically, centers initiate recirculation and can be employed to attract/retain particles [63,64] and mix fluids, while saddles (and connecting streamlines) partition the flow, enabling particle separation and sorting [4,15] or spatially controlled chemistry [4,65]. Based on Fig. 2(g), we anticipate that inner rings, being tucked within the muscle, will be difficult to image experimentally. Further, repulsive (red) and attractive (blue) saddles, that lie along the axis of symmetry in unperturbed simulations, may not be found on the experimentally imaged midplane, as a consequence of muscle imperfections and perturbations induced by the aluminum rod. We also expect the ring's midplane to periodically displace away (few tens of microns) from the microscope's focusing plane, due to tissue contractions, leading to slight shifts in the imaged flow structures.

Thus, we identify in the two external center rings the likely most robustly detectable structures, persisting three-dimensionally [Fig. 2(c)] off the midplane and unobstructed by the muscle/rod presence. We then expect to observe, projected on the μPIV imaging plane, four centers, located around the muscle ring and associated with recirculatory flows.

Overall, we numerically find that muscle rings of approximately ∼3–4 mm inner diameter and ∼4–5 mm outer diameter may be appropriate candidates for streaming experimental measurements. Indeed, at typical oscillation amplitudes (∼100 μm) and frequencies (1–4 Hz), such rings are observed to generate streaming velocities (∼10 μm/s) significantly larger than background disturbances (∼1 μm/s). Further, key flow structures are predicted to closely surround the muscle, thus falling within a compact field of view, while remaining sufficiently separated for experimental detection.

Autonomous streaming. We grow the biostreamer targeting the computationally identified guidelines. A PDMS toroidal mold of 5 mm inner diameter, 12 mm outer diameter, and 3 mm depth is fabricated, and the mixture of wild-type C2C12 cells and ECM is seeded [Fig. 1(a)]. Mold dimensions are determined to account for the shrinking associated with muscle compaction and differentiation. Based on our experience and previous characterizations of muscle tissue compaction [25], upon maturation and release from the mold [Fig. 1(a)] we expect ∼60% and ∼20% reductions in outer and inner diameter, respectively, leading to muscles of desired geometry (∼3–4 mm inner, ∼4–5 mm outer diameters [42]), as indeed observed in Figs. 2(h) and 2(i). Further, confocal fluorescent imaging [Fig. 2(h)] confirms the myotubes circumferential alignment, thus enabling radial contraction.

Upon transfer to the μPIV system, the ring's specific dimensions and spontaneous contraction amplitudes/frequencies are determined by the software Tracker [66] by averaging top and bottom edge displacements across 1000 camera images acquired at 50 Hz. In Figs. 2(h)–2(n) we show a muscle ring of 3.5 mm inner diameter, 4.7 mm outer diameter, 1.4 mm tissue depth, 3.1 Hz dominant contraction frequency, and 72 μm/117 μm average peak-to-peak top/bottom amplitudes. These values are typical, approximately within 10% of the average measurements across our samples, as illustrated in Table S1 and Fig. S5 [42]. Obtained amplitudes and frequencies are reflected in the kymographs (generated from ImageJ [42,67]) of Fig. 2(j),

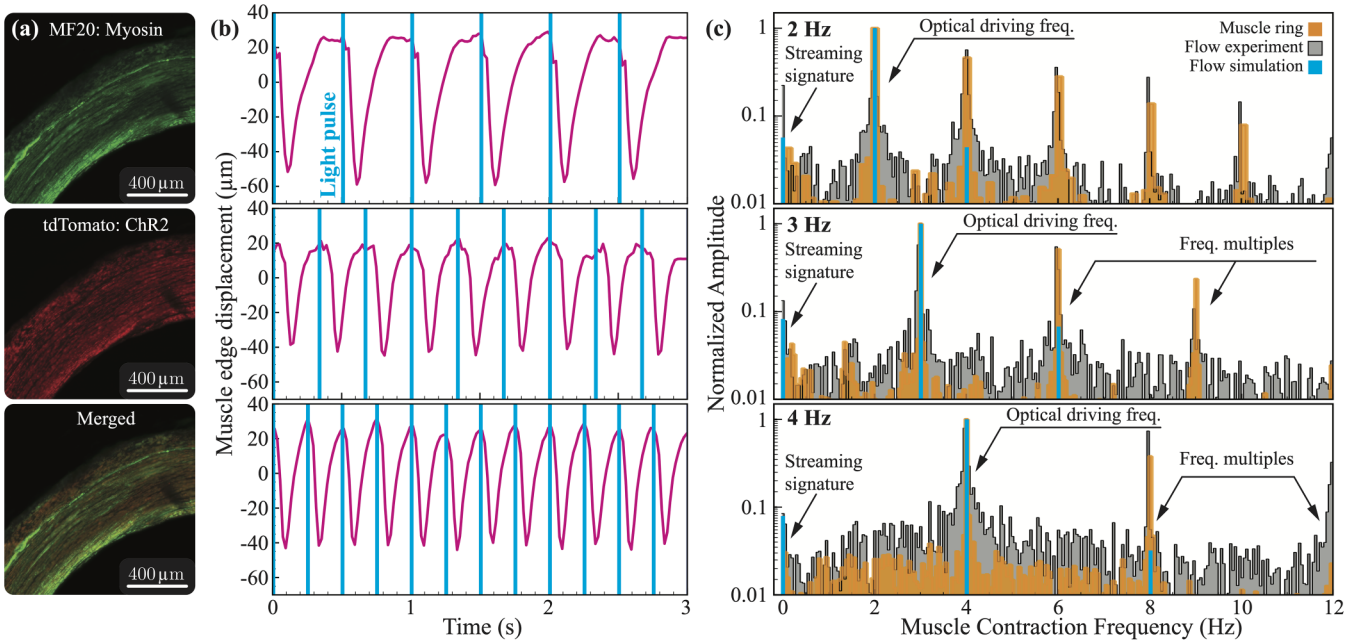

FIG. 3. Optically controlled streaming. (a) Confocal fluorescent z-stack images of a section of a muscle ring showing the myotubes (MF 20, green) and the ChR2 marker (tdTomato, red) at the same locations. (b) Muscle edge displacement of the top half of the muscle ring over 3 s (pink) and corresponding light stimulation pattern made of pulses of 10 ms duration (blue) at different frequencies. (top) 2 Hz stimulation results in an average peak-to-peak amplitude of 81 µm, (middle) 3 Hz stimulation, and 59 µm peak-to-peak amplitude, and (bottom) 4 Hz stimulation and 61 µm peak-to-peak amplitude. (c) Frequency spectrum of the experimental flow (u), simulated flow, and muscle actuation at optical driving frequencies of (top) 2 Hz, (middle) 3 Hz, and (bottom) 4 Hz. The normalized amplitude is presented on a logarithmic scale.

over 2 s, and in the time-varying edge displacements of Fig. 2(k), over 4 s. We note that the top/bottom tracked edges exhibit asymmetric trajectories and a slight phase difference in their periodic motion [Fig. 2(k)]. While these effects, attributed to the muscle fibers' inhomogeneity, do not appreciably affect the streaming fields observed in this study, the exploration of richer flow topologies generated by explicitly engineered phase differences remains a future avenue for research.

To facilitate comparison, we input these muscle-specific parameters into our simulations and analyze both experimentally and computationally obtained flows. We first consider experimental steady streamlines, depicted in Fig. 2(l) (top half). These are obtained by averaging recorded instantaneous velocities in the midplane, over eight contraction cycles. This procedure removes (approximately) the flow's oscillatory component, revealing the underlying rectified, steady streaming field. We also note that time averaging helps mitigate (although not entirely remove) the effect of cyclic disturbances, such as the periodic shifting of the ring's midplane due to the contractions of the tissue. As anticipated, we observe two distinct centers and corresponding flow recirculation regions. These features are also visible in the mirrored streaming field obtained from simulations, revealing close agreement [Fig. 2(l), bottom half]. We note the slight asymmetry that characterizes experiments, on account of ring geometry and actuation imperfections as well as due to the presence of the aluminum rod. These perturbations, together with the aforementioned subtle shift of the ring's midplane, are also likely responsible for the missing NSS along the ring axis of symmetry, features that we previously identified as nonrobustly observable. We further highlight how in experiments, centers are found closer to the biostreamer than in simulations. This is consistent with the intuition that wall effects, due to the aluminum enclosure, would result in flow geometric compression. Finally, we note that the overall streaming response is found to be robust (consistent with previous demonstrations [7,8,44,68]), with associated features seen across cyclic muscle contractions and samples (Fig. 3 and the Supplemental Material [42]). While the above analysis confirms that the shape of the flow observed experimentally is consistent with computational predictions, we remark here that the strength of the flow is also consistent. Indeed, as discussed in detail in the Supplemental Material [42], measured and simulated velocity magnitudes are found to be of the same order of magnitude ($\sim$10 µm/s).

To confirm that these flow features are indeed the result of a streaming process, we proceed with identifying additional hallmarks of streaming through a combination of proper orthogonal decomposition (POD) [69] and flow spectral analyses. POD considers space-time correlations in the velocity field and extracts energetic coherent structures lingering in the flow, information that can be employed to determine sampling locations for subsequent spectral analysis. On account of the streaming flow being a second-order effect, this procedure allows us to identify flow locations of likely favorable signal-to-noise ratios, minimizing the effects of undesirable disturbances. We thus consider experimental and simulated midplane velocities over 20 s, extract the corresponding dominant POD mode [Fig. 2(m), 90% of total energy, orange/blue intensity correlates to local flow energy], and sample it at different coordinates (within high-energy regions) at which

spectral analysis of raw velocity data is performed [Fig. 2(m) and Supplemental Fig. 3 [42]].

In the frequency domain, streaming flows present a well-known signature: a driving-frequency main peak capturing first-order $O(\epsilon)$ oscillatory effects, a zero-frequency peak (about 10 times smaller) capturing second-order $O(\epsilon^2)$ streaming rectification, and a series of peaks of exponentially decaying magnitude at multiples of the driving frequency, corresponding to increasingly higher-order effects [1]. Our data are found to quantitatively recapitulate this structure, as illustrated in Fig. 2(n), where we report the spectra of measured (black) and simulated (blue) velocities at the representative location marked in Fig. 2(m). Additionally, for reference, we plot the spectrum of the muscle top edge displacement (orange) of Fig. 2(k). As can be noticed, the measured/simulated flows indeed respond to the input muscle frequency (peak at 3.1 Hz) and produce rectification (peak at 0 Hz). The relative magnitude of these two peaks is also in line with theory, with rectification about one order of magnitude weaker, on account of being a second-order effect.

We further note the presence of the characteristic peaks at multiples of the driving frequency. In simulations (blue bars), as expected from theory, the peak corresponding to the first frequency doubling (∼6 Hz) presents a magnitude comparable to the rectification peak, consistent with the fact that this is also a second-order effect. Remaining frequency-multiple peaks are also detected from simulated flows (see Fig. 2 of the Supplemental Material [42]), although they are not visible in Fig. 2(n) given their negligible normalized amplitudes (that fall below the plotted lower bound), on account of their exponential decay [1].

The experimental flow response (black bars) does present a similar structure, whereby driving, rectification, and cascading peaks are all found at the theoretically and computationally expected frequencies. However, the relative magnitudes of the peaks at driving-frequency multiples are stronger than predicted. This is not necessarily surprising for the following complementary reasons. First, the muscle is soft and can deform in response to the flow, unlike in theory where the body is considered to be rigid or in simulations where the ring's deformations are imposed. Disregarding body compliance leads to underestimating the strength of the streaming response, as recently demonstrated in [8,44] where flow-induced elastic deformations are shown to provide an additional source of streaming. Second, frequency multiples might also originate from the tissue on account of its own mechanical rectification response to a driving oscillatory forcing (in this case cyclic contractions), through a mechanism mathematically similar to fluids [1]. This effect, pertaining to the solid phase, might then couple with the flow, strengthening both responses. That a combination of these factors may be at play here is suggested by the muscle power spectrum (orange bars) of Fig. 2(n), whereby deformations are found to precisely sync with the flow, presenting a set of highly structured harmonics that are unlikely to be the result of spontaneous, higher-frequency tissue contractions. While a rationale for the observed peak enhancement is provided, dissecting the exact mechanisms at play is beyond the scope of this work and not strictly necessary to confirm the presence of streaming and the potential utility of our bio-hybrid platform.

Thus, given the observed qualitative and quantitative agreement between experiments, simulations, and theory, we conclude that our tissue-engineered biostreamer is indeed capable of producing inertial flow rectification autonomously.

Optically controlled streaming. Now, we demonstrate controllability of the native function of the muscle ring by exploiting muscle contractions in response to an external light stimulus. To control the actuation frequency using optical stimulation, we fabricate our biostreamer following the same process of the autonomous streamer, however, we now utilize optogenetic C2C12 myoblasts. After fabrication, we use confocal fluorescence microscopy to confirm the expression of ChR2 after differentiation. As can be seen in Fig. 3(a), we observe the persistent expression of ChR2 within the tissue and, therefore, expect the muscle ring to respond to an external light stimulation of wavelength 470 nm [70]. An optical fiber, held 3 mm above the muscle ring by a clamp [Fig. 1(b)], is used to uniformly illuminate the tissue within the enclosure. The fiber delivers 10 ms pulses from the connected laser diode source at driving frequencies of 2, 3, and 4 Hz. These driving frequencies are less than, equal to, and greater than the autonomous biostreamer actuation frequency (∼3 Hz).

Upon light stimulation, the muscle ring of Fig. 3 (a different sample from Fig. 2) is observed to contract robustly for all three driving frequencies, as quantified by tracking its edge displacement Fig. 3(b). At the lowest driving frequency (2 Hz), the muscle actuation response is characterized by rapid contractions (∼0.1 s) followed by slower relaxations (∼0.4 s) to its original configuration [Fig. 3(b), top]. At higher driving frequencies (3 and 4Hz), the muscle responds to the stimulus consistently, with contractions over ∼0.1 s [Fig. 3(b), middle/bottom]. However, the relaxation time ($\leqslant$0.2 s) is no longer sufficient for returning to the original configuration, and smaller edge displacement amplitudes are realized. For the driving frequencies of 2, 3, and 4 Hz, the average peak-to-peak edge displacements are measured to be 81, 59, and 61 μm, respectively.

Using the same spectral analysis approach of Fig. 2, we characterize the oscillatory and rectified flow fields generated by the optically driven biostreamer, in both simulations and experiments. For all driving frequencies, we find that the experimental flow (black) responds with hallmarks similar to the spontaneous case, with the dominant mode shifting to align with the optical driving frequency [Fig. 3(c)], underscoring the system controllability. Further, and importantly, the zero-frequency peak, which corresponds to the rectified streaming flow, is observed for all three driving frequencies. In good agreement with theory and simulations (blue), the magnitude of the zero-frequency peak is one order of magnitude smaller than the dominant mode. Moreover, the presence of the cascading peaks at multiples of the driving frequency is observed for all three cases. Specifically, for a driving frequency of 2 Hz, peaks of decaying magnitude are observed at 4, 6, 8, and 10 Hz. Similarly, for driving frequencies of 3 and 4 Hz, peaks of decaying magnitudes are observed at 6 and 9 Hz, and at 8 and 12 Hz, respectively. As for the autonomous biostreamer, the magnitude of the cascading peaks is larger in experiments than simulations, for the same reasons previously described.

IV. CONCLUSION

We have presented a bio-hybrid setup that allows us to investigate viscous streaming in biologically powered, untethered, 3D, and millimeter-scale systems, approximating conditions experienced by a host of small aquatic creatures, long speculated (but not confirmed) to autonomously rectify surrounding flows.

By combining tissue engineering, microparticle image velocimetry, numerical simulations, and flow analysis, we designed and demonstrated muscle-ring devices that, once freely suspended in bulk liquid, generate viscous streaming, autonomously or in a remotely controlled fashion, via light stimulation. This experimentally supports the hypothesis of millimeter-scale organisms powering and sustaining streaming. It also expands the range of functionalities currently afforded by bio-hybrid technology, equipping future biological robots with inertial rectification capabilities for local flow manipulation. In this regard, bio-fabrication advances will be needed to achieve higher muscle contraction frequencies, to overcome limited streaming flow speeds. This may be achieved by using gene editing tools or cell culturing techniques to bias muscle fibers toward fast twitching phenotypes, or by employing altogether different muscle cells which naturally possess higher actuation frequencies, such as arthropod fast excitatory muscles [71,72]. Finally, this work also illustrates the potential utility of bio-hybrid platforms, combined with simulations, for biophysics and fluid mechanics research.

ACKNOWLEDGMENTS

The authors thank S. Hilgenfeldt for helpful discussions over the course of this work. The authors acknowledge support from the National Science Foundation under NSF Elements Award No. OAC-2209322 (M.G.) and the NSF Expedition 'Mind in Vitro' Award No. IIS–2123781 (M.G., T.S.).

Z.D., Z.L., Y.B., F.K.C., G.J., M.T.A.S., L.P.C., and M.G. designed and performed the research; Z.D., Z.L., O.A., K.Y.H., and H.K. contributed to the physical realization of the bio-hybrid setup. Z.D., L.H., S.C., Y.B., and F.K.C. analyzed data. All authors wrote the paper.

[1] J. Holtsmark, I. Johnsen, T. Sikkeland, and S. Skavlem, Boundary layer flow near a cylindrical obstacle in an oscillating, incompressible fluid, J. Acoust. Soc. Am. **26**, 26 (1954).

[2] C. Lane, Acoustical streaming in the vicinity of a sphere, J. Acoust. Soc. Am. **27**, 1082 (1955).

[3] A. Bertelsen, A. Svardal, and S. Tjøtta, Nonlinear streaming effects associated with oscillating cylinders, J. Fluid Mech. **59**, 493 (1973).

[4] B. R. Lutz, J. Chen, and D. T. Schwartz, Microfluidics without microfabrication, Proc. Natl. Acad. Sci. USA **100**, 4395 (2003).

[5] B. R. Lutz, J. Chen, and D. T. Schwartz, Hydrodynamic tweezers: 1. Noncontact trapping of single cells using steady streaming microeddies, Anal. Chem. **78**, 5429 (2006).

[6] B. R. Lutz, J. Chen, and D. T. Schwartz, Microscopic steady streaming eddies created around short cylinders in a channel: Flow visualization and stokes layer scaling, Phys. Fluids **17**, 023601 (2005).

[7] Y. Bhosale, G. Vishwanathan, G. Upadhyay, T. Parthasarathy, G. Juarez, and M. Gazzola, Multicurvature viscous streaming: Flow topology and particle manipulation, Proc. Natl. Acad. Sci. USA **119**, e2120538119 (2022).

[8] S. Cui, Y. Bhosale, and M. Gazzola, Three-dimensional soft streaming, J. Fluid Mech. **979**, A7 (2024).

[9] F. K. Chan, Y. Bhosale, T. Parthasarathy, and M. Gazzola, Three-dimensional geometry and topology effects in viscous streaming, J. Fluid Mech. **933**, A53 (2022).

[10] Y. Bhosale, T. Parthasarathy, and M. Gazzola, Shape curvature effects in viscous streaming, J. Fluid Mech. **898**, A13 (2020).

[11] T. Parthasarathy, F. K. Chan, and M. Gazzola, Streaming-enhanced flow-mediated transport, J. Fluid Mech. **878**, 647 (2019).

[12] D. Klotsa, M. R. Swift, R. Bowley, and P. King, Interaction of spheres in oscillatory fluid flows, Phys. Rev. E **76**, 056314 (2007).

[13] D. Klotsa, M. R. Swift, R. Bowley, and P. King, Chain formation of spheres in oscillatory fluid flows, Phys. Rev. E **79**, 021302 (2009).

[14] P. Marmottant and S. Hilgenfeldt, A bubble-driven microfluidic transport element for bioengineering, Proc. Natl. Acad. Sci. USA **101**, 9523 (2004).

[15] R. Thameem, B. Rallabandi, and S. Hilgenfeldt, Particle migration and sorting in microbubble streaming flows, Biomicrofluidics **10**, 014124 (2016).

[16] C. Wang, S. V. Jalikop, and S. Hilgenfeldt, Size-sensitive sorting of microparticles through control of flow geometry, Appl. Phys. Lett. **99**, 034101 (2011).

[17] S. Ookawara, N. Oozeki, K. Ogawa, P. Löb, and V. Hessel, Process intensification of particle separation by lift force in arc microchannel with bifurcation, Chem. Eng. Proc.: Proc. Intensif. **49**, 697 (2010).

[18] R. Thameem, B. Rallabandi, and S. Hilgenfeldt, Fast inertial particle manipulation in oscillating flows, Phys. Rev. Fluids **2**, 052001 (2017).

[19] G. Vishwanathan and G. Juarez, Steady streaming viscometry of Newtonian liquids in microfluidic devices, Phys. Fluids **31**, 041701 (2019).

[20] G. Vishwanathan and G. Juarez, Inertial focusing in planar pulsatile flows, J. Fluid Mech. **921**, R1 (2021).

[21] T. A. Spelman and E. Lauga, Arbitrary axisymmetric steady streaming: Flow, force and propulsion, J. Eng. Math. **105**, 31 (2017).

[22] W. Gilpin, M. S. Bull, and M. Prakash, The multiscale physics of cilia and flagella, Nat. Rev. Phys. **2**, 74 (2020).

[23] O. Aydin *et al.*, Neuromuscular actuation of biohybrid motile bots, Proc. Natl. Acad. Sci. USA **116**, 19841 (2019).

[24] J. Wang *et al.*, Computationally assisted design and selection of maneuverable biological walking machines, Adv. Intell. Syst. **3**, 2000237 (2021).

[25] G. J. Pagan-Diaz *et al.*, Simulation and fabrication of stronger, larger, and faster walking biohybrid machines, Adv. Funct. Mater. **28**, 1801145 (2018).

[26] R. Raman *et al.*, Optogenetic skeletal muscle-powered adaptive biological machines, Proc. Natl. Acad. Sci. USA **113**, 3497 (2016).

[27] Y. Kim *et al.*, Remote control of muscle-driven miniature robots with battery-free wireless optoelectronics, Sci. Robot. **8**, eadd1053 (2023).

[28] S.-J. Park *et al.*, Phototactic guidance of a tissue-engineered soft-robotic ray, Science **353**, 158 (2016).

[29] K. Y. Lee *et al.*, An autonomously swimming biohybrid fish designed with human cardiac biophysics, Science **375**, 639 (2022).

[30] B. J. Williams, S. V. Anand, J. Rajagopalan, and M. T. A. Saif, A self-propelled biohybrid swimmer at low Reynolds number, Nat. Commun. **5**, 3081 (2014).

[31] Y. Morimoto, H. Onoe, and S. Takeuchi, Biohybrid robot powered by an antagonistic pair of skeletal muscle tissues, Sci. Robot. **3**, eaat4440 (2018).

[32] Y. Akiyama *et al.*, Atmospheric-operable bioactuator powered by insect muscle packaged with medium, Lab Chip **13**, 4870 (2013).

[33] Z. Li *et al.*, Biohybrid valveless pump-bot powered by engineered skeletal muscle, Proc. Natl. Acad. Sci. USA **116**, 1543 (2019).

[34] Z. Li *et al.*, Adaptive biohybrid pumping machine with flow loop feedback, Biofabrication **14**, 025009 (2022).

[35] Y. Akiyama, A. Nakayama, S. Nakano, R. Amiya, and J. Hirose, An electrical stimulation culture system for daily maintenance-free muscle tissue production, Cyborg Bionic Syst. **2021**, 9820505 (2021).

[36] W. C. Drennan, O. Aydin, B. Emon, Z. Li, M. S. H. Joy, A. Barishman, Y. Kim, M. Wei, D. Denham, A. Carrillo, and M. T. A. Saif, A forward-engineered muscle tissue driven soft robotic swimmer, bioRxiv (2024) .

[37] E. Ko *et al.*, Empowering engineered muscle in biohybrid pump by extending connexin 43 duration with reduced graphene oxides, Biomaterials **287**, 121643 (2022).

[38] N. R. de Barros *et al.*, Enhanced maturation of 3d bioprinted skeletal muscle tissue constructs encapsulating soluble factor-releasing microparticles, Macromol. Biosci. **23**, 2300276 (2023).

[39] K. Deisseroth, Optogenetics, Nat. Methods **8**, 26 (2011).

[40] R. Raman, C. Cvetkovic, and R. Bashir, A modular approach to the design, fabrication, and characterization of muscle-powered biological machines, Nat. Protoc. **12**, 519 (2017).

[41] G. J. Pagan-Diaz *et al.*, Engineering geometrical 3-dimensional untethered in vitro neural tissue mimic, Proc. Natl. Acad. Sci. USA **116**, 25932 (2019).

[42] See Supplemental Material at http://link.aps.org/supplemental/10.1103/4fzg-vn1v for details on fabrication of the PDMS mold; methods for engineering the cell culture and the muscle ring; details on hydrogel tube formation; elaboration for the experimental setup; procedures for tracking muscle displacements; details on muscle ring staining; lighting requirements for inducing muscle contractions in transfected cells; methods and implementation of the numerical simulation; details on postprocessing of simulation results, including proper orthogonal decomposition and spectral analysis; comparison of flow strengths obtained through simulation and experiments.

[43] N. Riley, Steady streaming, Annu. Rev. Fluid Mech. **33**, 43 (2001).

[44] Y. Bhosale, T. Parthasarathy, and M. Gazzola, Soft streaming–flow rectification via elastic boundaries, J. Fluid Mech. **945**, R1 (2022).

[45] D. Neal, M. S. Sakar, L.-L. S. Ong, and H. H. Asada, Formation of elongated fascicle-inspired 3D tissues consisting of high-density, aligned cells using sacrificial outer molding, Lab Chip **14**, 1907 (2014).

[46] O. Aydin *et al.*, Development of 3D neuromuscular bioactuators, APL Bioeng. **4**, 016107 (2020).

[47] S. G. Uzel, A. Pavesi, and R. D. Kamm, Microfabrication and microfluidics for muscle tissue models, Prog. Biophys. Mol. Biol. **115**, 279 (2014).

[48] E. Bell, B. Ivarsson, and C. Merrill, Production of a tissue-like structure by contraction of collagen lattices by human fibroblasts of different proliferative potential in vitro, Proc. Natl. Acad. Sci. USA **76**, 1274 (1979).

[49] D. P. Hart, The elimination of correlation errors in piv processing, in *9th International Symposium on Applications of Laser Techniques to Fluid Mechanics* (Citeseer, Lisbon, Portugal, 1998), pp. 13–16.

[50] R. D. Keane, and R. J. Adrian, Theory of cross-correlation analysis of PIV images, Appl. Sci. Res. **49**, 191 (1992).

[51] M. S. Sakar *et al.*, Formation and optogenetic control of engineered 3D skeletal muscle bioactuators, Lab Chip **12**, 4976 (2012).

[52] J. B. Bryson *et al.*, Optical control of muscle function by transplantation of stem cell–derived motor neurons in mice, Science **344**, 94 (2014).

[53] N. C. Klapoetke *et al.*, Independent optical excitation of distinct neural populations, Nat. Methods **11**, 338 (2014).

[54] T. Okano, S. Satoh, T. Oka, and T. Matsuda, Tissue engineering of skeletal muscle. highly dense, highly oriented hybrid muscular tissues biomimicking native tissues, ASAIO J. **43**, M749 (1997).

[55] T. A. Gwyther *et al.*, Engineered vascular tissue fabricated from aggregated smooth muscle cells, Cells Tissues Organs **194**, 13 (2011).

[56] M. Gazzola, P. Chatelain, W. M. Van Rees, and P. Koumoutsakos, Simulations of single and multiple swimmers with non-divergence free deforming geometries, J. Comput. Phys. **230**, 7093 (2011).

[57] Y. Bhosale, T. Parthasarathy, and M. Gazzola, A remeshed vortex method for mixed rigid/soft body fluid–structure interaction, J. Comput. Phys. **444**, 110577 (2021).

[58] M. Gazzola, W. M. Van Rees, and P. Koumoutsakos, C-start: Optimal start of larval fish, J. Fluid Mech. **698**, 5 (2012).

[59] M. Gazzola, C. Mimeau, A. A. Tchieu, and P. Koumoutsakos, Flow mediated interactions between two cylinders at finite Re numbers, Phys. Fluids **24**, 043103 (2012).

[60] M. Gazzola, B. Hejazialhosseini, and P. Koumoutsakos, Reinforcement learning and wavelet adapted vortex methods for simulations of self-propelled swimmers, SIAM J. Sci. Comput. **36**, B622 (2014).

[61] M. Gazzola, A. A. Tchieu, D. Alexeev, A. de Brauer, and P. Koumoutsakos, Learning to school in the presence of hydrodynamic interactions, J. Fluid Mech. **789**, 726 (2016).

[62] S. H. Strogatz, *Nonlinear Dynamics and Chaos: With Applications to Physics, Biology, Chemistry, and Engineering* (CRC Press, 2018).

[63] K. Chong, S. D. Kelly, S. Smith, and J. D. Eldredge, Inertial particle trapping in viscous streaming, Phys. Fluids **25**, 033602 (2013).

[64] K. Chong, S. D. Kelly, S. T. Smith, and J. D. Eldredge, Transport of inertial particles by viscous streaming in arrays of oscillating probes, Phys. Rev. E **93**, 013109 (2016).

[65] B. R. Lutz, J. Chen, and D. T. Schwartz, Characterizing homogeneous chemistry using well-mixed microeddies, Anal. Chem. **78**, 1606 (2006).

[66] D. Brown, W. Christian, and R. M. Hanson, Tracker video analysis and modeling tool (version 6.1.5) (2023), https://www.compadre.org/osp/items/detail.cfm?ID=7365 .

[67] J. Schindelin *et al.*, Fiji: An open-source platform for biological-image analysis, Nat. Methods **9**, 676 (2012).

[68] S. Agarwal, F. K. Chan, B. Rallabandi, M. Gazzola, and S. Hilgenfeldt, An unrecognized inertial force induced by flow curvature in microfluidics, Proc. Natl. Acad. Sci. USA **118**, e2103822118 (2021).

[69] L. Sirovich, Analysis of turbulent flows by means of the empirical eigenfunctions, Fluid Dyn. Res. **8**, 85 (1991).

[70] J. Y. Lin, M. Z. Lin, P. Steinbach, and R. Y. Tsien, Characterization of engineered channelrhodopsin variants with improved properties and kinetics, Biophys. J. **96**, 1803 (2009).

[71] S. Gordon and M. H. Dickinson, Role of calcium in the regulation of mechanical power in insect flight, Proc. Natl. Acad. Sci. USA **103**, 4311 (2006).

[72] R. K. Josephson, J. G. Malamud, and D. R. Stokes, Asynchronous muscle: A primer, J. Exp. Biol. **203**, 2713 (2000).